This is a repository copy of *Complex Faulting and Triggered Rupture During the 2018 MW 7.9 Offshore Kodiak, Alaska, Earthquake*.

White Rose Research Online URL for this paper:
http://eprints.whiterose.ac.uk/155115/

Version: Published Version

Article:

Complex Faulting and Triggered Rupture During the 2018 M$_W$ 7.9 Offshore Kodiak, Alaska, Earthquake

N. A. Ruppert[1] ![iD], C. Rollins[1] ![iD], A. Zhang[2], L. Meng[2] ![iD], S. G. Holtkamp[1], M. E. West[1] ![iD], and J. T. Freymueller[1] ![iD]

[1]Geophysical Institute, University of Alaska Fairbanks, Fairbanks, AK, USA, [2]Department of Earth, Planetary, and Space Sciences, UCLA, Los Angeles, CA, USA

Abstract We combine aftershock relocations, source mechanisms, teleseismic *P* wave backprojection, and Global Positioning System data inversion to constrain complex faulting geometry of the 2018 M$_W$ 7.9 offshore Kodiak earthquake. Relocated aftershocks delineate several N-S trends including a prominent 110-km-long segment, as well as broad NE-SW trends. Global Positioning System modeling and backprojection indicate that the NE-SW trending left-lateral strike-slip segments released most energy dominating far-field crustal deformation and radiated wavefield. Backprojection infers fast E-to-W rupture propagations superimposed on a slower S-to-N migration. We propose a five-segment model of the rupture that was partially driven by dynamic triggering.

Plain Language Summary In the early morning hours of 23 January 2018, a magnitude 7.9 earthquake struck ~300 km offshore Kodiak Island, Alaska, in the outer rise region of the Alaska-Aleutian subduction zone. While the moment tensor for the earthquake suggests predominantly strike-slip faulting, the true complexity of the source has only become evident through analysis of multiple data sets (aftershock locations and source mechanisms, Global Positioning System deformation, and teleseismic *P* wave backprojection). Our analysis indicates simultaneous rupture on a system of N-S and NE-SW oriented conjugate faults. The N-S faults correlate with plate bending faults imaged by seismic imaging and high-definition bathymetry. The NE-SW faulting trends do not coincide with locations of oceanic plate fractures but correlate with orientations of fault planes of previously recoded earthquakes in the area. Rupture propagation during the earthquake did not follow a continuous path and was partially driven by dynamic and static stress triggering. The modeling results indicate that left-lateral strike-slip segments released most energy thus dominating the radiated wavefield and the resulting crustal deformation. The Mw 7.9 offshore Kodiak earthquake is another example of a complex rupture of the oceanic lithosphere.

1. Introduction

In the early morning hours of 23 January 2018, a magnitude 7.9 earthquake struck ~300 km offshore Kodiak Island, Alaska, in the outer rise region of the Alaska-Aleutian subduction zone. While the moment tensor for the earthquake suggests predominantly strike-slip faulting, the true complexity of the source has only become evident through analysis of multiple data sets.

The Alaska-Aleutian subduction zone extends for ~3,800 km from the Gulf of Alaska westward to the Komandorsky Islands and accommodates relative motion between the Pacific and North American Plates. The characteristics of this tectonic boundary, such as convergence direction and rate, trench separation, and degree of coupling, vary widely along its extent (Freymueller et al., 2008). The nature of outer rise seismicity also changes along the arc: Typical normal faulting outer rise events are more common in the central and western Aleutians (west of 160°W) and nearly absent in the eastern Aleutians and southern Alaska (Christensen & Ruff, 1988). Very few earthquake source mechanisms are cataloged for the outer rise region offshore Kodiak. Those that do exist do not indicate a uniform pattern of faulting. An m$_b$ 5.4 event occurred a few months after the great 1964 M$_W$ 9.2 Alaska earthquake and featured typical outer rise normal faulting (Stauder & Bollinger, 1966). An M$_W$ 6.0 earthquake in 1999 east of the current sequence was a reverse faulting event and an M$_W$ 4.9 earthquake in 2017 was a strike-slip event with a similar focal mechanism to the 2018 M$_W$ 7.9 earthquake (Figure 1).
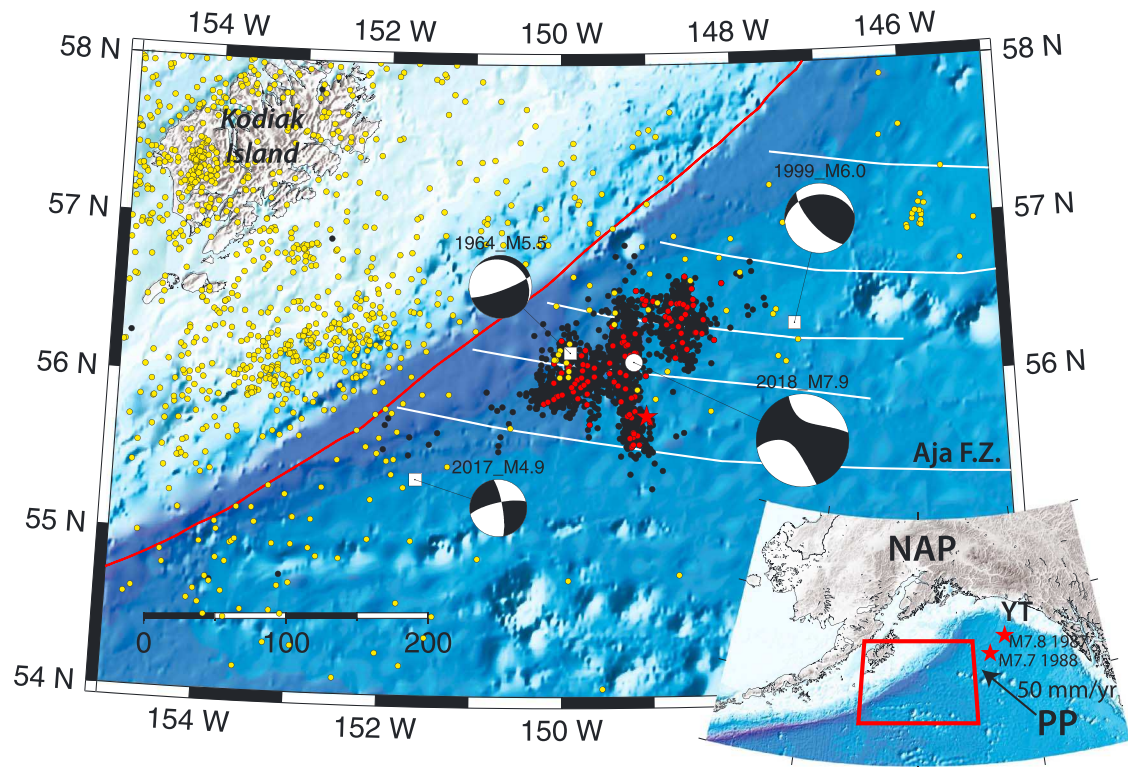
Figure 1. Regional map showing background seismicity ($M >= 3$, 1990–2017, yellow circles), 2018 aftershocks ($M >= 3$ and 4, black and red circles, respectively), moment tensors and locations of previously recorded events in the outer rise region (white squares) and the 23 January 2018 M_W 7.9 earthquake (circle indicates location of the centroid). Inferred fracture zones are shown by white lines, and the megathrust is marked by red line. Inset figure shows location of the study area within the regional frame and locations of the 1987–1988 Gulf of Alaska earthquakes (NAP = North American Plate; PP = Pacific Plate; YT = Yakutat Terrane).

A series M_W 7.2–7.8 strike-slip events occurred in the northeast Gulf of Alaska in 1987–1988 on a system of conjugate and parallel faults in an area with very little historic seismicity (Hwang & Kanamori, 1992; Lahr et al., 1988) (Figure 1, inset). However, seismic reflection data provide clear evidence that these faults were active long before the earthquake sequence began (Reece et al., 2013). These events were followed by more examples of complex faulting in oceanic lithosphere. The 1998 M_W 8.1 Balleny Islands (Antarctic Plate) earthquake ruptured faults that did not correlate with any known features on the ocean floor and may have involved subevents on different fault planes (Henry et al., 2000). The 2000 M_W 7.8 Wharton Basin earthquake (off Sumatra) involved ruptures of both NS and EW trending fault planes during the mainshock (Abercrombie et al., 2003; Robinson et al., 2001). The 2004 M_W 8.1 Tasman Sea earthquake reactivated old structures with a new mechanism, rupturing an old spreading ridge in a strike-slip event (Robinson, 2011). More recently, the 2012 Wharton Basin sequence involved multiple $M > 8$ subevents within a complex set of faults intersecting at highly oblique angles (Meng et al., 2012).

These examples are a reminder that the far-field observations are often an aggregate over a series of subfaults. The studies above suggest that this may be particularly common in oceanic crust, where the preexisting fabric may not necessarily align with the dominant stress directions. In these cases, stress release might be most easily accommodated through a complex set of subfault ruptures instead of occurring along a single canonical fault line.

Several fracture zones have been identified in the vicinity of the 2018 offshore Kodiak Island earthquake such as the Aja Fracture Zone to the south (Matthews et al., 2011; Pitman III & Hayes, 1968). In addition, seismic reflection and high-resolution bathymetry have revealed numerous approximately N-S trending faults (Reece et al., 2013), which were interpreted as preexisting fractures in the Pacific Plate spreading fabric that have been reactivated as predominately normal plate bending faults by Pacific Plate subduction. This sea floor fabric bears striking resemblance to that imaged in the Wharton Basin region (Singh et al., 2017).
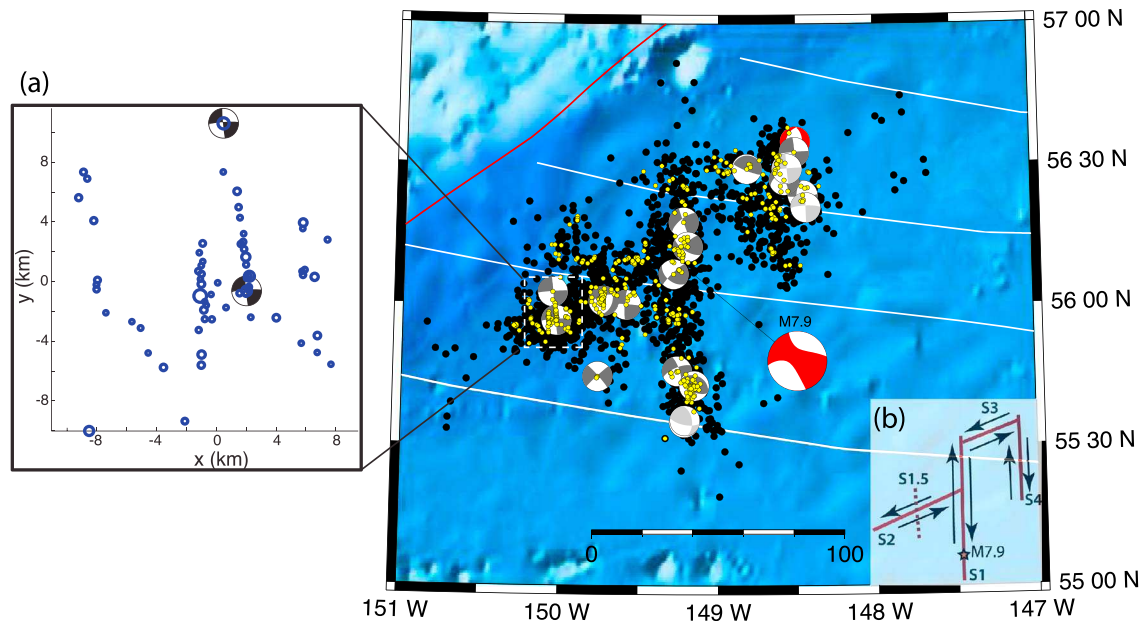
Figure 2. Map of the aftershocks and moment tensors: black = $M > =3$ aftershocks from Alaska Earthquake Center catalog, yellow = relocated aftershocks. Gray beach balls are from National Earthquake Information Center ComCat catalog (M_W 4.1–5.1), and red beach balls are the centroid moment tensors from global CMT catalog for the mainshock and the largest aftershock (M_W 5.5, 24 January 00:04 UTC). Inset map (a) shows a subset of relocated aftershocks that demonstrates right-lateral faulting along NS trending faults. Inset (b) shows a proposed fault segment model.

We combine analysis of the aftershock locations, seismic moment tensors, teleseismic *P* wave backprojection, and Global Positioning System (GPS) displacements to constrain complex faulting during the 23 January 2018 M_W 7.9 earthquake.

2. Methods and Results

2.1. Aftershock Relocations and Source Mechanisms

The Alaska Earthquake Center analyzed over 2,800 aftershocks through the end of March 2018. Due to the offshore location, the magnitude of completeness is higher than that of the catalogs on land, at $M = 3.0$. The aftershocks illuminate a complex network of ruptured subfaults (Figure 2).

To better resolve aftershock locations, we employ the earthquake relocation technique GrowClust (Trugman & Shearer, 2017). First, we subset the catalog to include earthquakes with $M > 3.3$, resulting in 515 events. Eliminating the smallest magnitude events improves computational efficiency and removes the most poorly constrained events. Using *hypoddpy* (Krishner, 2015), for each aftershock we link up to 20 neighboring events that have at least four phase arrivals in common at nearby seismic stations. This produces 6,239 event pairs with an average offset of ~8 km between linked events (on the order of the location uncertainty for these offshore events). In total, >90,000 *P* phase and >28,000 *S* phase pairs are selected, band-pass filtered from 1 to 5 Hz, and 5 s of data are extracted around each phase (-1 to +4 s) prior to cross correlation. The resulting cross correlations are used as input to the GrowClust program. Within GrowClust, we use a maximum station distance of 600 km, a maximum root-mean-square residual of 1 s to join clusters, and a minimum of five events required to perform a cluster shift test. We allow earthquakes within 20-km catalog distance and 15-km relocated distance to join clusters and allow up to 10 km of shift. These parameters result in 420 earthquakes being relocated, with root-mean-square differential time residuals of ~1 s for both *P* and *S* phases.

We used 14 moment tensor solutions from National Earthquake Information Center ComCat catalog that range in magnitudes between M_W 4.1 and 5.1 and centroid moment tensor (CMT) solutions from global CMT catalog for the mainshock and the largest aftershock (M_W 5.5, 24 January 00:04 UTC).

The overall aftershock distribution illuminates several sharp N-S and broad NE-SW trends (Figure 2). We identified four distinct aftershock groups associated with possible fault planes labeled as S1–S4 in Figure 2b. The
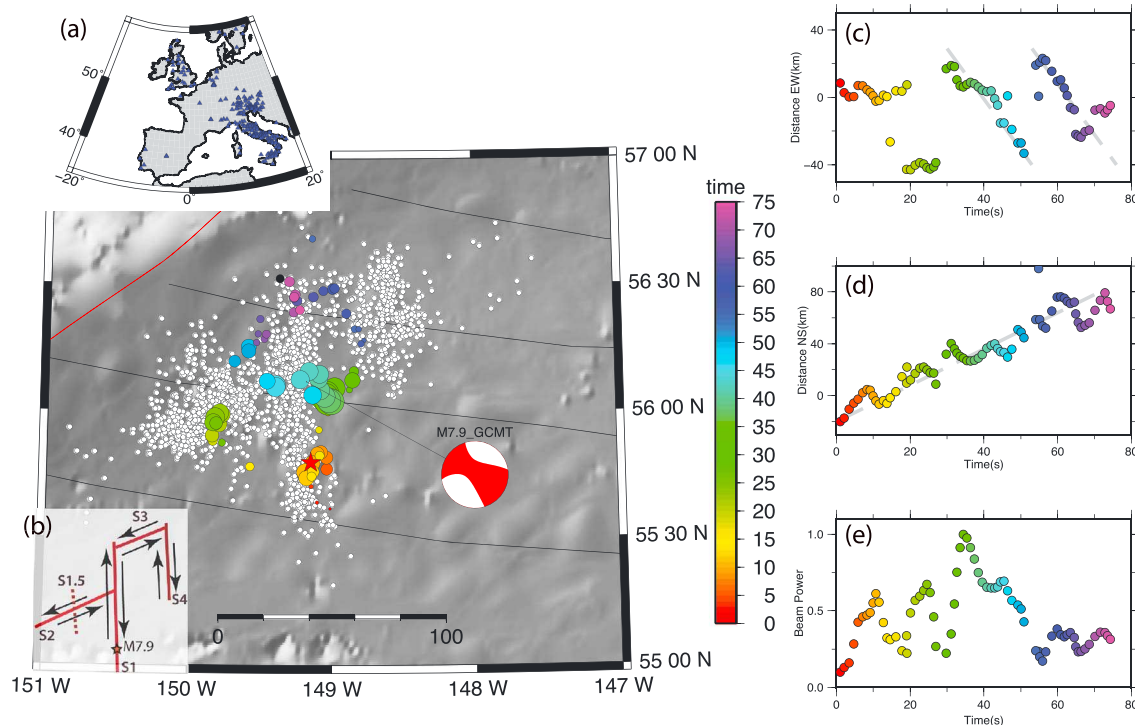
Figure 3. Kinematic rupture process revealed by teleseismic *P* wave backprojection. The circles are color coded by time and sized by power (see panel e) to represent the location of high-frequency radiators at different time frame. Red star is the M$_W$ 7.9 epicenter, and white circles are *M* > =3 aftershocks. Inset map (a) shows distribution of stations used for backprojection. Inset (b) shows a proposed fault segment model. (c) Rupture distance along the EW direction (positive distance indicates rupture to the east of the hypocenter); dashed lines are reference rupture speed of 3 km/s. (d) Rupture distance along the NS direction (positive distance indicates rupture to the north of the hypocenter); the dashed line indicates reference rupture speed of 1.4 km/s. (e) Beam power of the radiators as a function of time. GCMT = global centroid moment tensor.

most prominent is the 110-km-long N-S trend S1 with the mainshock epicenter located near its southern end. Neither catalog nor relocated aftershocks indicate a single, well-defined E-W striking trend. Instead, epicenters in the region west of S1 are distributed over a broad NE-SW trending zone (S2) and form several clear N-S streaks ~10 km long (Figure 2a). Focal mechanisms for aftershocks along these streaks show right-lateral strike-slip faulting. There is also a broad 70-km-long NS aligned cluster northeast of the main S1 segment (S4). However, no connecting structure between the main segment and this northeast segment is clear in the aftershock locations (S3).

The focal mechanisms for aftershocks within S1 and S4 segments predominantly indicate right-lateral strike-slip motion. A cluster of reverse faulting aftershocks is concentrated near the southern end of the main S1 lineation. These are located just north of the identified fracture zone and may indicate rupture interaction with this structural barrier. One of the only two normal faulting aftershocks is associated with the S4 after-shock cluster and indicates NS-fault planes (it was the largest aftershock). The second normal faulting aftershock is located in the middle of the S2 segment and indicates a west or SW trending fault plane. Its location is close to the m$_b$ 5.5 normal faulting event in 1964.

2.2. Teleseismic *P* Wave Backprojection

We backprojected teleseismic *P* waves recorded at 298 broadband stations in continental Europe to image the kinematic rupture process of the M$_W$ 7.9 mainshock (Figure 3a). The backprojection technique utilizes very few prior assumptions on fault parametrization, Green's functions, or rupture velocity and thus can robustly constrain the spatiotemporal evolution, rupture extent, and rupture speed of large complex earthquakes (Fan & Shearer, 2016; Ishii et al., 2005; Meng et al., 2012; Wang et al., 2016; Zhang et al., 2012). In this study, we adopted the Multitaper-MUSIC array processing technique that provides superior resolution to separate closely spaced sources (Meng et al., 2011). We collected
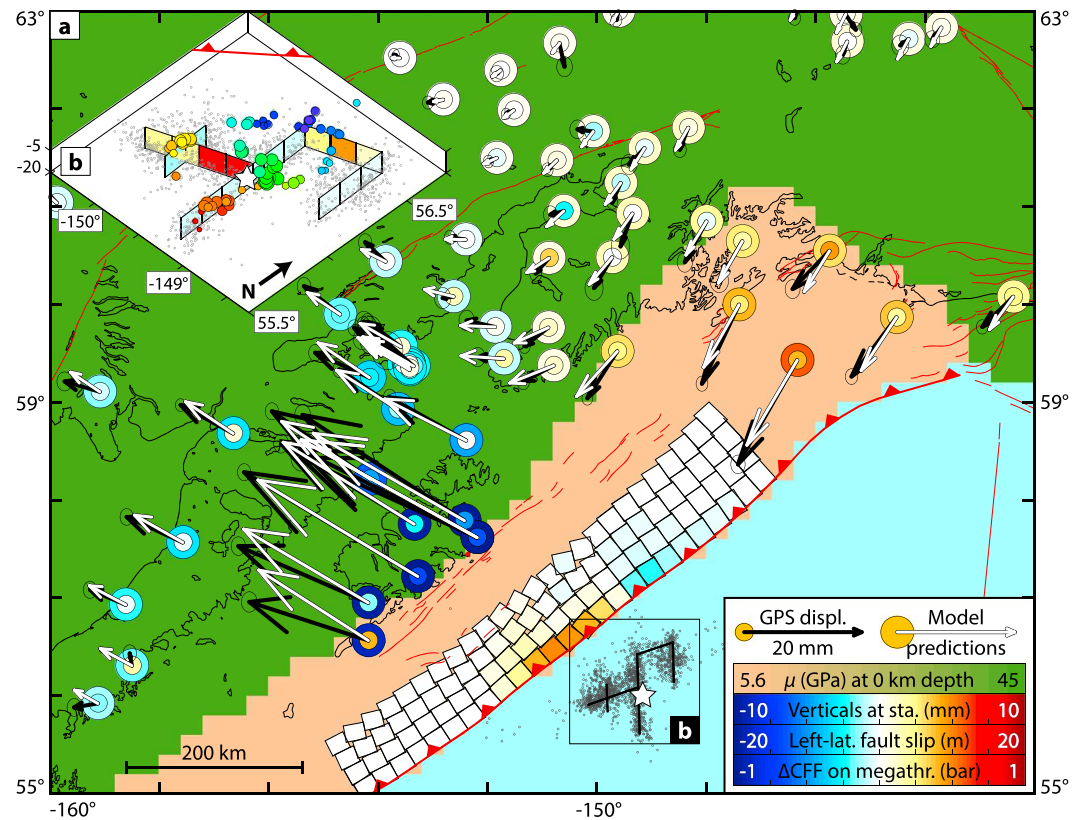
Figure 4. Observed and modeled static GPS displacements (a) and estimated slip on fault segments (b). Black arrows and small colored circles are observed horizontal and vertical displacements. White arrows and large colored circles are model-predicted horizontal and vertical displacements. Warm colors indicate uplift at GPS stations in (a) and left-lateral slip on segments in (b); cool colors indicate subsidence and right-lateral slip. Gray points are aftershocks. Background beige color represents accretionary prism in the model; green represents lithosphere. Red lines are faults (Koehler et al., 2012). Also shown are Coulomb stress changes imparted to the megathrust. (b) Three-dimensional view of inferred slip distribution. Gray points are aftershocks; colored circles are high-frequency radiators from backprojection (Figure 3). GPS = Global Positioning System.

coherent waveform data from the ORFEUS data center (http://orfeus-eu.org/webdc3/). The seismograms are filtered in the band of 0.5 to 2 Hz and empirically aligned with the first 5 s of the *P* wave arrivals. This correction procedure assumes that the first arrivals originated from the hypocenter (Ishii et al., 2005) and provides a static correction of travel time due to 3-D path effects. The aligned data are then backprojected using a 1-D reference velocity model to pinpoint when and where difference source regions were radiating energy.

The results suggest complex conjugate ruptures and segmentation along several faults trending approximately NS and approximately EW—observations that are remarkably consistent with the aftershock locations (Figure 3). The earthquake initiated as a relatively low energy bilateral rupture along a NS trending fault (S1) near its southern end with the first notable energy burst at around 10 s (Figures 3d and 3e). Between 20 and 30 s, the rupture leaps ~60 km NW from the earthquake epicenter (S1.5 segment, Figure 3c). From 30 to 50 s, the dominant release occurs along a continuous E-to-W trending path with a rupture speed of 3 km/s (S2 segment, Figure 3c). Beyond 50 s, radiators are less energetic. This late energy appears well constrained to a region north and east of the rest of the rupture. It likely represents another fault segment near the northern end of S1 with the strike in the westerly direction and predominant propagation path from east to west (S3). The rupture speed on S3 is around 3 km/s, similar to that on S2 (Figure 3c). The aftershock locations clearly image a 70-km-long NS oriented fault segment (S4), which corresponds to high-frequency (HF) radiators at around and after 65 s. Beyond 75 s, backprojection is no longer viable because the teleseismic *P* waves lack coherency. The overall rupture extent is ~100 km in the NS direction, which is consistent with the aftershock

zone extent. The average NS rupture speed is (~1.4 km/s), is lower than the two EW ruptures. The rupture pattern is overall highly complex, as inferred for the previous oceanic plate events.

2.3. GPS Modeling

Following the offshore Kodiak earthquake, University NAVSTAR Consortium made available a data set of processed coseismic displacements at Plate Boundary Observatory GPS stations in Alaska (Figure 4). We first explore whether the GPS displacement field could have been produced by slip on the north striking faults. We build a slip model consisting of segments S1, S1.5, and S4 and estimate the final static coseismic slip on these segments from the horizontal and vertical GPS displacements using a Monte Carlo method assuming a homogeneous half-space Earth model, all slip planes vertical, slip pure right-lateral, and strike 0° (supporting information Text S1). The horizontal displacements predicted by the resulting slip model show a systematic azimuthal misfit to the horizontal GPS displacements (Figure S1). The inferred slip model and misfit do not improve by assuming that the segments have a westward dip (Figure S2) or allowing for a normal component of slip (Figure S3). We next add segments S2 and S3 to the model; to reduce the number of free parameters, we assume again that all segments are vertical and restrict slip to be pure right lateral on S1, S1.5, and S4 and pure left lateral on S2 and S3. We test different values for the strike of S2 and S3 (Figures S4–S7). The resulting models fit the GPS significantly better than those with only the north striking segments, but all have unconvincing attributes. Some models feature the highest slip at the far northeast of the aftershock distribution (Figure S4 and S5), where backprojection indicates minimal HF radiation, while the other features a less one-sided slip distribution but underpredicts the displacements at stations to the northeast (Figure S7). Allowing for nonvertical dips again does not change the inferred slip or the misfit (Figure S6). This suggests that the displacements may have been proportionally amplified by an aspect of the earthquake or setting that the homogeneous half-space model does not account for.

To assess whether this effect may have been related to heterogeneous elastic properties, we construct a 3-D Earth model of the southern Alaska margin that includes the Prince William Complex, an accretionary wedge that likely extends from the trench to the southeast coast of Kodiak (Plafker et al., 1994; Figure 4, supporting information Text S2, and Figures S8 and S9). Elastostatic modeling suggests that this sedimentary wedge may have acted like a cushion: Compared to a homogeneous Earth model, it would damp the displacements on Kodiak relative to those northeast of the earthquake (Figure S10), producing the apparent proportional amplification of the latter in the GPS displacements. Incorporating this heterogenous model into the inversion where S2 and S3 strike 253° yields a slip distribution that is more consistent with the distribution of HF radiators (Figure 4b) and brings the predicted displacements on the northeast into a better agreement. We thus choose this as our preferred GPS-based model (Figure 4b). Most of the slip is inferred on the segments S2 and S3, and indeed, an inversion using only those segments fits the GPS nearly as well as the five-segment model (Figure S11) The total coseismic moment release in the GPS-based model (computed as the sum of $S \cdot A \cdot \mu$, where S is the slip, A is the area of each patch, and μ is the shear modulus along each patch, here 45 GPa as per the heterogeneous Earth model) is equivalent to a $M_w = 7.81$ earthquake. We calculate (supporting information Text S3) that this slip distribution would have imparted a Coulomb stress increase of ~0.5 bar to the Alaska subduction zone along the nearby trench (Figure 4).

3. Discussion

The 2018 M_w 7.9 Offshore Kodiak earthquake is another example of a complex rupture of the oceanic lithosphere. The source complexity is evidenced by the aftershock distribution, which extends over a $>100 \times 100$-km region and includes several well-defined N-S lineations but no clear E-W trends. At the same time, GPS modeling of crustal deformation and finite source modeling with teleseismic recordings (https://earthquake.usgs.gov/earthquakes/eventpage/us2000cmy3#finite-fault) favor left-lateral faulting on faults striking south of west. The backprojection results presented in this study also support complex rupture model featuring rupture in both N-S and E-W directions.

P wave first-motion analysis, location of the epicenter, and backprojection results all point to the rupture initiation as a right-lateral strike-slip earthquake on a N-S oriented fault plane, with predominant propagation to the north, but also some propagation to the south. However, instead of simply continuing along this faulting plane, the rupture bifurcated into a left-lateral strike-slip conjugate fault plane
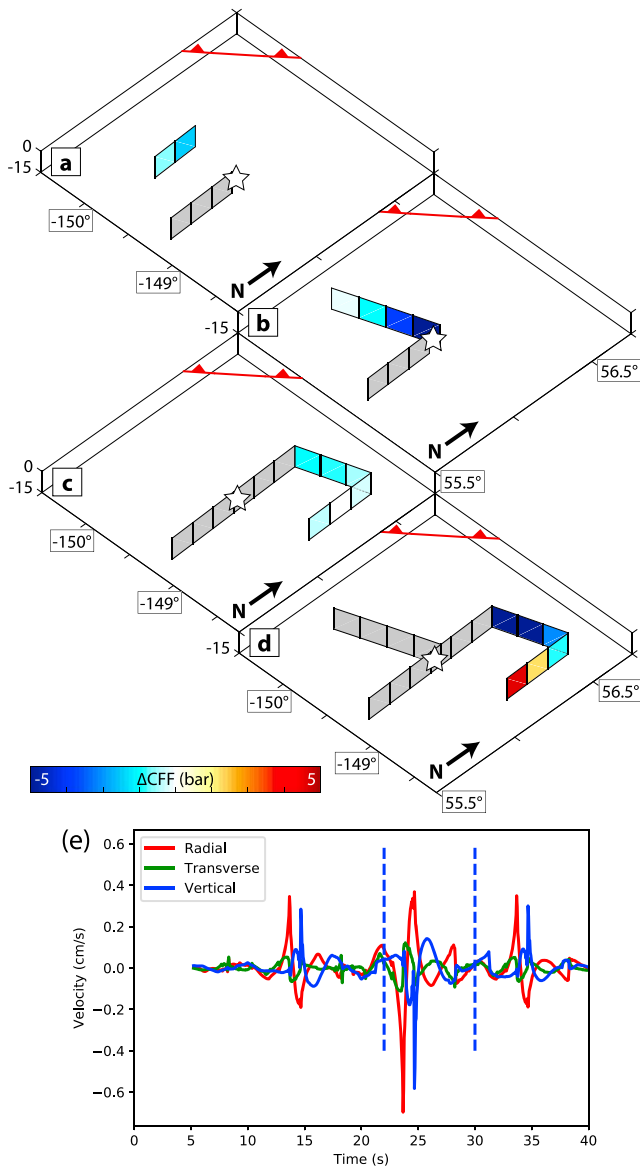
Figure 5. Results of the static and dynamic stress triggering tests. Progressive Coulomb stress changes throughout the rupture. Stress changes imparted by slip on (a) the southern half of S1 to S1.5; (b) the southern half of S1 to S2; (c) the full length of S1 to S3 and S4; (d) S1 and S2 to S3 and S4. (e) Synthetic three-component velocity seismograms recorded at 55.95°N, 149.82°W. The blue dashed line marks the timing of the high-frequency radiators of back projection on subfault S2.

westward. The most energetic backprojection radiators coincide with the location of the global CMT near the point where the two proposed planes would intersect (Figure 3). The GPS modeling also required significant motions on this westerly trending fault plane (Figure 4 and supporting information). At the same time, a number of smaller right-lateral strike-slip ruptures were triggered along NS oriented plate bending faults (Figure 2a).

Additional complication of the rupture process occurred between 20 and 30 s when the HF radiators suddenly shifted 60 km NW of the epicenter to a region that is seemingly disconnected from the main rupture propagation (Figure 3).

To test triggering mechanisms during the mainshock rupture, we compute the progression of static Coulomb and dynamic stress. We use the elastic component of RELAX (Barbot & Fialko, 2010a, 2010b) to compute Coulomb stress changes between subfaults using the fault segments and slip distribution in the preferred GPS model (Figure 4) assuming a shear modulus of 45 GPa, a Poisson's ratio of 0.25, and an effective friction coefficient of 0.4 (King et al., 1994). We again assume that slip is pure right-lateral and pure left lateral on the north striking and SW trending fault segments, respectively. We find that progressive Coulomb stress changes throughout the rupture are predominantly negative and would have inhibited failure (Figures 5a–5c), reminiscent of the 2012 Wharton Basin earthquake, which twice ruptured into compressional quadrants (Meng et al., 2012). The only positive stress changes are those on segment S4 following the ruptures of segments S1 and S2 (Figure 5d), which could have conceivably promoted failure on that segment at that point in the rupture. The results otherwise do not suggest static triggering as a plausible mechanism for the propagation and diffusion of the rupture, and so we turn to dynamic triggering.

To address the effect of dynamic triggering from S1 to S1.5 and S2, we compute the synthetic three-component velocity seismograms using the frequency-wavenumber integral method (Zhu & Rivera, 2002). Moment tensor of S1 and the fault orientation of S2 are taken from the global CMT inversion (Figure 3). Figure 5e is an example of the seismogram at (55.95°N, 149.82°W), where we see the cluster of HF radiators on S1.5 and S2. The amplitudes of the radial component are more pronounced than the transverse component, suggesting that Rayleigh waves play a dominant role of triggering the rupture. Moreover, the timing of the radiators on HF matches with the pulses of the seismogram. According to Jaeger and Cook (1979), peak dynamic stress can be inferred from the velocity:

$$\sigma_d = Gu/v_s \tag{1}$$

where G is the shear modulus, u is the peak velocity, and v_s is the phase velocity. In this study, we use a shear modulus of 30 GPa and a constant Rayleigh waves velocity of 3.5 km/s (Miyazawa & Brodsky, 2008). The peak ground velocity is about 0.78 cm/s, and the corresponding peak stress change is around 0.67 bar, above the threshold of triggering of around 0.1 bar (Brodsky & Prejean, 2005; Hill & Prejean, 2015). Therefore, the HF radiators observed on S1.5 and S2 can be dynamically triggered by the Rayleigh wave radiated from S1.

In summary, we hypothesize that the dynamic stress change played a significant role in triggering N-S subfault rupture S1.5 ahead of the main rupture front reaching that area and promoted westerly bifurcation of the rupture onto a conjugate fault plane S2. The static stress changes were significant enough to possibly promote the rupture of S4.

4. Conclusions

Complex faulting of the 2018 M_W 7.9 offshore Kodiak earthquake involves simultaneous rupture on a system of N-S and NE-SW oriented conjugate faults. The N-S faults correlate with plate bending faults imaged by seismic imaging and high-definition bathymetry (Reece et al., 2013). The NE-SW faulting trends do not coincide with locations of oceanic plate fractures but correlate with orientations of fault planes of previously recoded earthquakes in the area. Rupture propagation during the earthquake did not follow a continuous path and was partially driven by dynamic and static stress triggering. We propose a model with five ruptured subfaults. The teleseismic P wave backprojection and GPS modeling results indicate that NE-SW trending left-lateral strike-slip segments released most energy thus dominating the radiated wavefield and the resulting crustal deformation.

References

Abercrombie, R., Anatolik, M., & Ekstrom, G. (2003). The June 2000 Mw 7.9 earthquake south of Sumatra: Deformation in the India-Australia plate. *Journal of Geophysical Research*, *108*(B1), 2018. https://doi.org/10.1029/2001JB000674

Barbot, S., & Fialko, Y. (2010a). Fourier-domain Green's function for an elastic semi-infinite solid under gravity, with applications to earthquake and volcano deformation. *Geophysical Journal International*, *182*(2), 568–582. https://doi.org/10.1111/j.1365-246X.2010.04655.x

Barbot, S., & Fialko, Y. (2010b). A unified continuum representation of postseismic relaxation mechanisms: Semi-analytic models of afterslip, poroelastic rebound and viscoelastic flow. *Geophysical Journal International*, *182*(3), 1124–1140. https://doi.org/10.1111/j.1365-246X.2010.04678.x

Brodsky, E. E., & Prejean, S. G. (2005). New constraints on mechanisms of remotely triggered seismicity at Long Valley caldera. *Journal of Geophysical Research*, *110*, B04302. https://doi.org/10.1029/2004JB003211

Christensen, D. H., & Ruff, L. J. (1988). Seismic coupling and outer rise earthquakes. *Journal of Geophysical Research*, *93*(B11), 13,421–13,444. https://doi.org/10.1029/JB093iB11p13421

Fan, W., & Shearer, P. M. (2016). Fault interactions and triggering during the 10 January 2012 Mw 7.2 Sumatra earthquake. *Geophysical Research Letters*, *43*, 1934–1942. https://doi.org/10.1002/2016GL067785

Freymueller, J. T., Woodard, H., Cohen, S. C., Cross, R., Elliott, J., Larsen, C. F., et al. (2008). Active deformation processes in Alaska, based on 15 years of GPS measurements. In J. T. Freymueller, et al. (Eds.), *Active tectonics and seismic potential of Alaska*, *Geophysical Monograph Series* (Vol. 179, pp. 1–42). Washington, DC: American Geophysical Union.

Henry, C., Das, S., & Woodhouse, J. H. (2000). The great March 25, 1998, Antarctic Plate earthquake: Moment tensor and rupture history. *Journal of Geophysical Research*, *105*(B7), 16,097–16,118. https://doi.org/10.1029/2000JB900077

Hill, D. P., & Prejean, S. G. (2015). Dynamic triggering. In H. Kanamori (Ed.), *Treatise on geophysics* (2nd ed., Vol. 4, chap. 8, pp. 273–304). Oxford, UK: Elsevier.

Hwang, L. J., & Kanamori, H. (1992). Rupture processes of the 1987-1988 Gulf of Alaska earthquake sequence. *Journal of Geophysical Research*, *97*(B13), 19,881–19,908. https://doi.org/10.1029/92JB01817

Ishii, M., Shearer, P. M., Houston, H., & Vidale, J. E. (2005). Extent, duration and speed of the 2004 Sumatra-Andaman earthquake imaged by the Hi-Net array. *Nature*, *435*(7044), 933–936. https://doi.org/10.1038/nature03675

Jaeger, J. C., & Cook, N. G. W. (1979). *Fundamentals of rock mechanics* (p. 593). London: Chapman and Hall.

King, G. P., Stein, R. S., & Lin, J. (1994). Static stress changes and the triggering of earthquakes. *Bulletin of the Seismological Society of America*, *84*(3), 935–953.

Koehler, R.D., Farrell, R.-E., Burns, P.A.C., & Combellick, R.A. (2012), Quaternary faults and folds in Alaska: A digital database (Sheet 1, scale 1:3,700,000, pp. 31).

Kreemer, C., Blewitt, G., & Klein, E. C. (2014). A geodetic plate motion and global strain rate model. *Geochemistry, Geophysics, Geosystems*, *15*, 3849–3889. https://doi.org/10.1002/2014GC005407

Krishner, L. (2015). hypoDDpy 1.0. *Zenodo*. https://doi.org/10.5281/zenodo.18907

Lahr, J. C., Page, R. A., Stephens, C. D., & Christensen, D. H. (1988). Unusual earthquakes in the Gulf of Alaska and fragmentation of the Pacific Plate. *Geophysical Research Letters*, *15*(13), 1483–1486. https://doi.org/10.1029/GL015i013p01483

Matthews, K. J., Muller, R. D., Wessel, P., & Whittaker, J. M. (2011). The tectonic fabric of the oceanic basins. *Journal of Geophysical Research*, *116*, B12109. https://doi.org/10.1029/2011JP008413

Meng, L., Ampuero, J.-P., Stock, J., Duputel, Z., Luo, Y., & Tsai, V. C. (2012). Earthquake in a maze: Compressional rupture branching during the 2012 Mw 8.6 Sumatra earthquake. *Science*, *337*(6095), 724–726. https://doi.org/10.1126/science.1224030

Meng, L., Inbal, A., & Ampuero, J.-P. (2011). A window into the complexity of the dynamic rupture of the 2011 Mw 9 Tohoku-Oki earthquake. *Geophysical Research Letters*, *38*, L00G07. https://doi.org/10.1029/2011GL048118

Miyazawa, M., & Brodsky, E. E. (2008). Deep low-frequency tremor that correlates with passing surface waves. *Journal of Geophysical Research*, *113*, B01307. https://doi.org/10.1029/2006JB004890

Neal, R. M. (2003). Slice sampling. *Annals of Statistics*, *31*(3), 705–767. https://doi.org/10.1214/aos/1056562461

Okada, Y. (1985). Surface deformation due to shear and tensile faults in a half-space. *Bulletin of the Seismological Society of America*, *75*(4), 1135–1154.

Pitman, W. C. III, & Hayes, D. E. (1968). Sea-floor spreading in the Gulf of Alaska. *Journal of Geophysical Research*, *73*(20), 6571–6580. https://doi.org/10.1029/JB073i020p06571

Plafker, G., Moore, J. C., & Winkler, G. R. (1994). Geology of the southern Alaska margin. In G. Plafker & H. C. Berg (Eds.), *The geology of Alaska*, *The Geology of North America* (Vol. G1, pp. 389–449). Boulder, CO: Geological Society of America.

Reece, R. S., Gulick, S. P. S., Christenson, G. L., Horton, B. K., Van Avendonk, H., & Barth, G. (2013). The role of farfield tectonic stress in oceanic intraplate deformation, Gulf of Alaska. *Journal of Geophysical Research: Solid Earth*, *118*, 1862–1872. https://doi.org/10.1002/jgrb.50177

Robinson, D. P. (2011). A rare great earthquake on an oceanic fossil fracture zone. *Geophysical Journal International*, *186*(3), 1121–1134. https://doi.org/10.1111/j.1365-246X.2011.05092.x

Robinson, D. P., Henri, C., Das, S., & Woodhouse, J. H. (2001). Simultaneous rupture along two conjugate planes of the Wharton Basin earthquake. *Science*, *292*(5519), 1145–1148. https://doi.org/10.1126/science.1059395

Singh, S. C., Hananto, N., Qin, Y., Leclerc, F., Avianto, P., Tapponnier, P. E., et al. (2017). The discovery of a conjugate system of faults in the Wharton Basin intraplate deformation zone. *Science Advances*, *3*(1), e1601689. https://doi.org/10.1126/sciadv.1601689

Stauder, W., & Bollinger, G. A. (1966). The focal mechanism of the Alaska earthquake of March 28, 1964, and its aftershock sequence. *Journal of Geophysical Research*, *71*(22), 5283–5296. https://doi.org/10.1029/JZ071i022p05283

Trugman, D. T., & Shearer, P. M. (2017). GrowClust: A hierarchical clustering algorithm for relative earthquake relocation, with application to Spanish Springs and Sheldon, Nevada, earthquake sequences. *Seismological Research Letters*, *88*(2A), 379–391. https://doi.org/10.1785/0220160188

Wang, D., Mori, J., & Koketsu, K. (2016). Fast rupture propagation for large strike-slip earthquakes. *Earth and Planetary Science Letters*, *440*, 115–126. https://doi.org/10.1016/j.epsl.2016.02.022

Zhang, H., Chen, J., & Ge, Z. (2012). Multi-fault rupture and successive triggering during the 2012 Mw 8.6 Sumatra offshore earthquake. *Geophysical Research Letters*, *39*, L22305. https://doi.org/10.1029/2012GL053805

Zhu, L., & Rivera, L. A. (2002). A note on the dynamic and static displacements from a point source in multilayered media. *Geophysical Journal International*, *148*(3), 619–627. https://doi.org/10.1046/j.1365-246X.2002.01610.x